Journal of Materials Chemistry

Cite this: *J. Mater. Chem.*, 2012, **22**, 9568

www.rsc.org/materials

PAPER

Geometrical confinement of quantum dots in porous nanobeads with ultraefficient fluorescence for cell-specific targeting and bioimaging†

Po-Jung Chen,[a] Shang-Hsiu Hu,[a] Wen-Ting Hung,[a] San-Yuan Chen*[a] and Dean-Mo Liu*[ab]

Received 5th January 2012, Accepted 27th February 2012
DOI: 10.1039/c2jm00080f

In this study, a new imaging mesoporous nanoparticle is reported with exceptionally efficient and stable fluorescence emission, which was constructed by embedding and stabilizing quantum dots (QDs) of different sizes into porous nanobeads, following a lipid-PEG_{2000}-COOH coating which was further encoded with cRGD targeting peptide through biotin–streptavidin bridges. The mesopores had ~10 nm diameter, were chemically modified, and facilitated internalization and stabilization of the QDs within the nanobeads upon the preparation protocol. Their outstanding optical contrasts render the highly fluorescent QDs as ideal fluorophores for wavelength-and-intensity multiplex color coding. The QDs tagged nanobeads showed optically strong and chemically stable imaging capability, both *in vitro* and *in vivo*, indicating powerful contrast modality among other alternatives. The cRGD-encoded lipid coated QDs tagged nanobeads (cRGD-encoded LQNBs) exhibited significantly increased $\alpha_v\beta_3$-expressing cell targeting toward MCF-7 breast cancer cells over the $\alpha_v\beta_3$-low expressing in HeLa cervix cancer cells, as confirmed by confocal laser scanning microscopy and flow cytometry. In MCF-7 xenograft nude mice, the cRGD-encoded LQNBs revealed prolonged accumulation time at the tumor site. In addition, the QNBs also demonstrated relatively high cell viability as compared to 3-mercaptopropionic acid (MPA)-functionalized QDs, indicating a successful design of highly-cytocompatible nanoparticulate platform capable of providing cell-specific targeting and nano-imaging modalities for biomedical applications.

Introduction

Design and fabrication of nanoobjects with sophisticated nanoscopic structures are technically important in advanced applications in areas including renewable energy,[1,2] biomedicine,[3,4] therapeutics,[5,6] complex materials and catalysis.[7–9] Composite structures integrating multi-functionalities in a given nanometric volume with elaborate advantages such as optical and electronic properties over their single constituent have been widely-studied topics in the recent decades.[10–13] One important strategy for construction of composite nanostructure is to introduce molecular, oligomeric or macromolecular precursors with self-assembled capability into the nanostructures.[14–18] However, most chemical modifications are complex, time-consuming and even at a risk of losing the original function of the starting nanomatrix. For example, optical probes such as quantum dots coated by silica, copolymer or lipids demonstrated a great damage of the quantum yield, approximately 30–50% lower than their original brightness, limiting their applications.[19,20] Furthermore, for biological applications, the optical probes should be stabilized between pH 4 and 8, a physiological range that has been frequently found in the human body. Therefore, the development of multifunctional nanoprobes enabling new imaging modalities beyond the intrinsic limitations of individual components is essential, and considerable attention has been devoted to a number of areas, ranging from fundamental biology to molecular imaging and medical diagnostics.

Recently, Gao *et al.*[21,22] have reported mesoporous silica and polystyrene microbeads encoded with quantum dots to maintain high fluorescence intensity and uniformity. The pore sizes are typically engineered to 30–100 nm for fast QD doping and uniform QD distribution inside the microbeads. A key factor contributing to the improved brightness is the multi-stage doping QDs and the inner pore chemical structures, which stabilizes QDs *via* physical adsorption and leads to nearly no sacrificing the optical properties. On the other hand, Tasciotti *et al.* and Ananta *et al.*[23,24] also reported porous micro-sized silica particles successfully doped with functional nanoparticles such as QDs, carbon nanotubes, Gd-based materials, or therapeutic agents through multi-stage modification, leading to a functionalized nanocarrier for imaging and biomedical use. Despite these recent achievements, a number of issues have addressed the limited

[a]*Department of Materials Sciences and Engineering, National Chiao Tung University, 1001 Ta Hsueh Road, Hsinchu, 300 Taiwan, ROC. E-mail: sanyuanchen@mail.nctu.edu.tw*
[b]*Institute of Traditional Medicine, College of Medicine, National Yang-Ming University, No.155, Sec.2, Linong Street, Taipei, 112 Taiwan, ROC. E-mail: deanmo_liu@yahoo.ca*
† Electronic supplementary information (ESI) available. See DOI: 10.1039/c2jm00080f

applications of this type of functionalized nanocarrier in biomedical research before its clinical translations. To a significant extent, size mismatch is one of the major reasons between current doped porous nanoobjects and the biological systems. On the length scale of micrometers, synthetic approaches based on silicon etching or chemical synthesis for making uniform nano-sized porous structures of tunable composition are well-established. However, a key problem is that the sizes of these mesoporous particles range from 1–10 μm, which are too big for applications such as molecular imaging, drug delivery, and biomolecular labeling. In addition, recent reports on mesoporous silica have demonstrated their feasibility for use in a variety of biological applications.[25–28] However, using a mesoporous silica matrix with a pore size of about 2∼3 nm to load guest molecules by a chemical bridge, will limit tagged large molecular weight molecules or particles and will damage the properties through the chemical bridge. Furthermore, the porous silica materials are less hydrophobic over both external and internal regions of the pores because of their highly hydrophilic groups *i.e.*, Si–O, Si–OH, distributed over the regions, which adversely affects the loading efficiency of many water insoluble active molecules of technical or therapeutic interest.

To overcome these problems, we employ QDs as the guest "molecule" internalized with nano-sized mesoporous silica nanoparticles, wherein a multifunctional nanoobject capable of imaging and targeting was constructed. This multifunctional nanocarrier was prepared *via* a facile, step-wise procedure, including (1) preparing a highly hydrophobic octadecyltrimethoxysilane-modified mesoporous silica nanoparticle (hydrophobic porous nanobeads) with a pore size greater than 10 nm, (2) internalizing hydrophobic QDs, and (3) bridging the peptide cRGD on the surface of QD-tagged nanobeads by using noncovalent biotin–streptavidin link rendering a potential cellular-based targeting achievable. The multifunctional nanocarrier designed in this work, to our knowledge, provides exceptionally high chemical and pH stability and in the meantime, offers a wide spectrum of multiplex color codings for targeting and imaging modality.

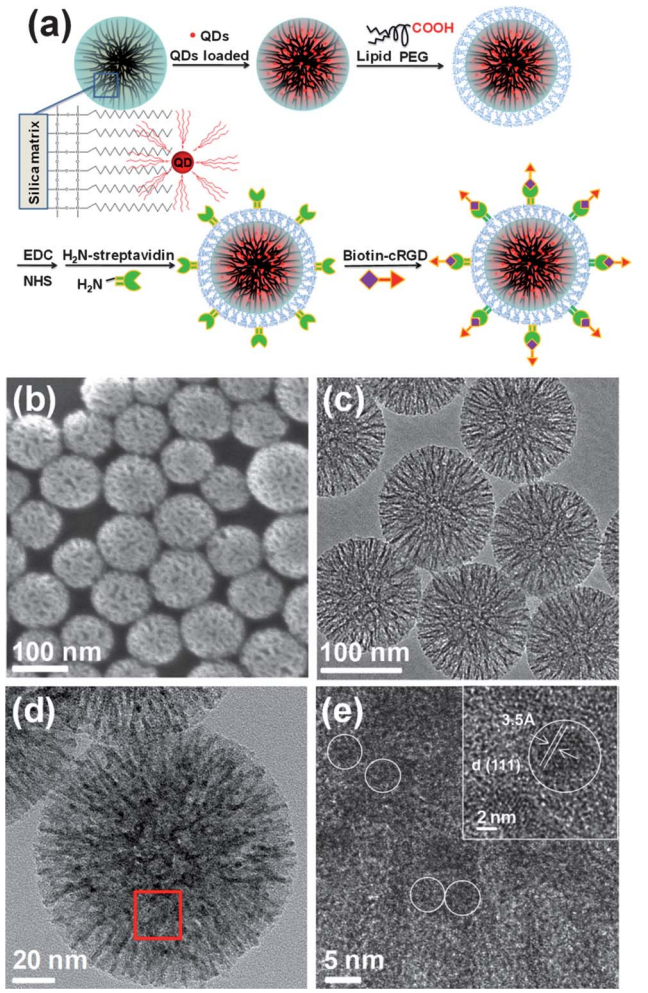

Fig. 1 (a) Schematic illustration of the synthesis and structure of the cRGD-encoded lipid coated quantum dots tagged porous nanobeads (cRGD-encoded LQNBs). (b) SEM image and (c) TEM image of porous nanobeads. (d) TEM image and the red box indicated (e) ha igh resolution TEM image of QDs tagged porous nanobeads. The circles indicated the QDs. The inset shows a lattice spacing of 3.5 Å for the CdSe (111) plane.

Results and discussion

Fig. 1a illustrates the synthesis of quantum dots (QDs) tagged porous nanobeads through a biotin–streptavidin bridged cRGD peptide. The first step is to synthesize the porous silica nanobeads with functionalized octadecyltrimethoxysilane (C_{18} hydrocarbon chain). The morphology and particle size of the porous nanobeads were analyzed with scanning and transmission electron microscopy as shown in Fig. 1b and 1c, respectively. A highly porous particle with an average size of 120 nm in diameter was observed. The N_2 adsorption/desorption isotherms of the nanobeads showed a relatively large surface area of 819.15 $m^2\ g^{-1}$ with Brunauer–Emmett–Teller (BET) analysis and a pore size of 5.28 nm (radius) on average was obtained using the Barret–Joiner–Halenda (BJH) method (Fig. S1).† The QDs were chemically anchored *via* hydrophobic interactions between the C_{18} hydrocarbon chain and trioctylphosphine oxide (TOPO) molecules, and tagging occurs when the hydrocarbon and surfactant molecules (both are flexible molecules) were intermolecularly inserted to form a stable, interdigitated configuration. Fig. 1d and 1e indicate the nanobeads decorated with QDs (black dots) show lattice patterns in the high resolution TEM images. The incorporation of quantum dots (QNBs) was further evidenced using elemental mapping and energy-dispersive X-ray spectroscopy by TEM (Fig. S2).† The C_{18} hydrocarbon chain modified not only the surface but also the inner porosity of the nanobeads, wherein the QDs were efficiently localized and stabilized within the porous nanobeads *via* chemical anchorage. In contrast, in the absence of chemical modification, the QDs aggregated outside of the porous nanobeads and the solution also showed fluorescence color (Fig. S3a and c),† indicating the QDs remained in the solution, rather than being localized inside the nanobeads. Furthermore, the QNBs were coated with functionalized lipid-PEG_{2000}-COOH to give carboxylic acid along the nanobead surface and consequently changed the surface from hydrophobic to hydrophilic. Furthermore, the formation of amide bonds between the carboxylic acids and amines was catalyzed by 1-ethyl-3-(3-dimethylaminopropyl) carbodiimide which activated the carboxyl

groups on the linkers to form O-*urea* derivatives. The addition of *N*-hydroxysuccinimide catalyzed the formation of the intermediate active esters that further reacted with the amine of the streptavidin to give the amide bond between the streptavidin and the carboxyl group along the surface of nanobeads. Finally, the cRGD-PEG_2-biotin was used to form a noncovalent biotin–streptavidin bridge on the surface of the lipid-PEG_{2000}-COOH coated QNBs (LQNBs). The QDs were incorporated within the pores in a rapid manner by strong hydrophobic interactions and a negligibly small amount of QDs (less than 0.1%) was left in the free solution after 2 h of impregnation.

Fig. 2a shows the loading efficiency of QDs in the nanobeads in terms of the emission character of QDs. The loading efficiency (LE %) of QNBs is determined using eqn (1):

$$\text{LE } \% = A/B \tag{1}$$

where A is the fluorescence intensity of QNBs at a specific time, and B is the fluorescence intensity of saturated QNBs loading. In this work, the fluorescence intensity of QNBs remained unchanged after 2-h impregnation, indicating a complete uptake of the QDs into the nanobeads. Fig. 2a showed similar loading efficiency profiles but a diverse loading amount. In the early-phase uptake, the QNBs emitting at 530 nm showed a higher loading efficiency than others because of their smaller size, which is easier accessible for the porous structure of the nanobeads. Different-sized QDs show different emission spectra, for example, QDs emitted at 530, 560 and 600 nm with the particle size ranging from approximately 3, 4 and 5 nm, respectively. Thus, the 530-nm emitting QDs were much smaller in size than the 600-nm emitting QDs, which was translated into a faster loading rate for the 530-nm emitting QDs than the others at the early-phase uptake. However, after 1 h of QD uptake, the emission intensity of the three encapsulated QDs approached an equilibrium status and appeared to reach a maximum emission after ta 2-h uptake with no further increase in loading efficiency. This finding also proved an efficient loading of the QDs *via* hydrophobic interactions between the hydrocarbon and TOPO molecules.

Once being loaded, the leakage of the QDs was determined by exposing to various diluting media included water, ethanol and butanol for 24 h. The inset of Fig. S4† showed good suspension of the QNBs in these solvents after 24 h and were then centrifuged to separate the QNBs from the diluting media. The resulting supernatants were colorless under UV exposure, whilst the collected QNBs showing red–orange appearance. From the photoluminescence spectrum, no detectable fluorescence intensity of the supernatants from those solutions was observed, indicating the QDs were readily chemically stabilized within the nanobeads (Fig. S4).† The distribution of the QDs in the nanobeads was also examined, since aggregation of QDs causes problems such as spectral broadening, self-quenching, and wavelength shifting of the resulting design. Fig. 2b shows the emission spectra, *i.e.*, orange–red-, yellow- and green-emitting QNBs, where the optical images of QNBs with three different emission appearances were clearly displayed. Besides, the quantum yield of the GNBs was determined experimentally. In comparison, we also prepared a number of quantum dots of the

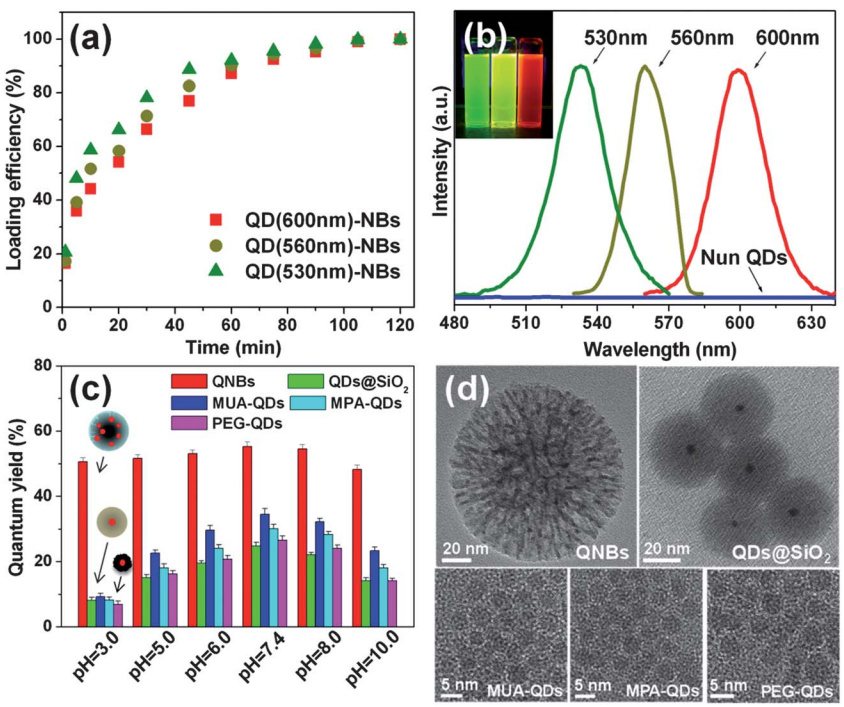

Fig. 2 (a) Loading efficiency profiles of QDs tagged the nanobeads within the soaking aqueous stock solution time by different emissions of QDs. (b) Fluorescence spectrum, showing three separated peaks (530, 560, and 600 nm) with nearly equal intensities. The inset shows three distinguishable emission colors of QNBs excited with a near-UV lamp. (c) The quantum yield comparison of QNBs, with traditional surface coatings, QDs@SiO_2, MUA-QDs, MPA-QDs and PEG-QDs dispersed in PH 3.0, 5.0, 6.0, 7.4, 8.0 and 10.0. (d) TEM images of QNBs, QDs@SiO_2, MUA-QDs, MPA-QDs and PEG-QDs.

same kind followed by surface modification with various materials according to literature reports.[29] As given in Fig. 2c and 2d, the QNBs illustrated the highest quantum yield (~55.2%) from all QDs coated with various materials, *e.g.*, the quantum yield for QDs@SiO_2, QDs functionalized 11-mercaptoundecanoic acid (MUA-QDs), QDs functionalized 3-mercaptopropionic acid (MPA-QDs) and QDs functionalized polyethylene glycol (PEG-QDs) was determined to be 24.8 34.5, 30.1 and 26.6%, respectively. One of the plausible reasons is the QDs were localized within the nanobeads the least in surface coverage with C_{18} ligands (through chemical linkages). The nanobeads were modified with the C_{18} hydrocarbons, which was likely not only on the outer surface but also on the pore walls, thus inhibiting diffusion of water-soluble compounds affecting the QDs. In other words, the QDs exposed the largest surface area to the environment while preparing into a nanostructure presently designed in this work compared to other nanostructural morphologies, where the capping materials suppressed considerably the quantum efficiency. Concerning the effect of pH, the quantum yield of the surface-modified QDs included QDs@SiO_2, MUA-QDs, MPA-QDs and PEG-QDs, showed a significant quenching effect at low pH, whilst the QNBs retained a relatively high quantum yield, more than 48% at low pH, and high pH as well (pH 3 and 10). However, a slight decay in the quantum yield of the QNBs was observed at pH 10 which is due to chemical instability of the silica matrix in basic conditions. Therefore, the QDs stabilized inside the mesoporous silica matrix prepared under current study, achieved not only excellent chemical stability but also reached exceptionally high quantum efficiency among other alternative nanostructures. This finding indeed allows the QNBs to be potentially applicable to quantitative cellular and molecular imaging.

Concerning the wide versatility of the QNBs with various combinations of the QDs of different sizes tagged with the nanobeads, Fig. 3a shows the quantitative results obtained from three quantum dots (having green, yellow and red emissions) tagged into the nanobeads. The use of m intensity levels (0, 1, 2, … m) at n different wavelength of the quantum dots gives $(m^n - 1)$ color codes.[30] However, the actual coding capabilities are likely to be substantially lower because of spectral overlapping and signal noise. Thus, using 3–5 colors with five intensity levels (designating as 0, 1, 2, 3, 4), yielding approximately 100 to 3000 recognizable color codes is realistic. Following a number of QD combinations tagged with the nanobeads, Fig. 3b and Fig. S5† show 7 clear and distinguishable fluorescence emission colors observed from resulting QNBs excited with a UV lamp and separated peaks in the fluorescence spectrum. This simple combination opens a wide variety of imaging potential for biomedical uses.

The true-color fluorescence images of nanobeads tagged with QDs emitting at 530 (green), 560 (yellow) and 600 nm (orange-red) are shown in Fig. 3c. These QNBs were considered monochromatic because they were prepared using single-color QDs, and were mixed and spread on a glass surface for fluorescence imaging. Although only a single light source (UV lamp) was used for excitation, all the LQNBs were distinctly and clearly observed. To further testify the imaging capability of the nanobeads, an *in vivo* test was carried out using two types of LQNBs, each doped with green and red QDs, respectively, followed by

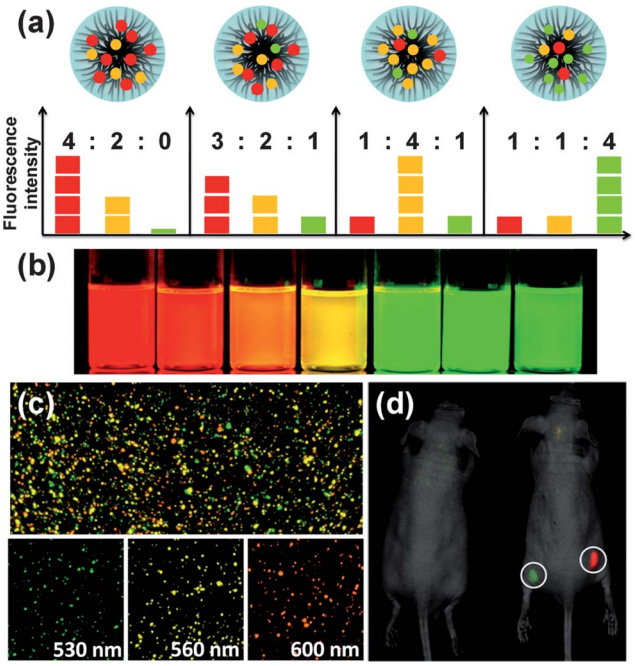

Fig. 3 (a) Schematic illustration of optical coding based on wavelength and intensity multiplexing. (b) Seven distinguishable emission colors of QNBs excited with a near-UV lamp. From left to right (red to green), the emission maxima are located at 598, 586, 575, 558, 549, 541 and 532 nm. (c) Fluorescence images of nanobeads doped with single-color QDs emitting light at 530 (green), 560 (yellow), and 600 nm (orange-red). (d) Two kinds emitting light of LQNBs, green and red QDs, subcutaneously injected into a nude mouse. The left nude mouse is without injection.

injecting into a nude mouse at two different locations for *in vivo* imaging detection, *via* a non-invasion *in vivo* imaging system (IVIS). As shown in Fig. 3d, the nude mouse at the left side, *i.e.*, the control group shows no detectable imaging contrast, whilst for the right-side group, a sharp contrast of the green and red imaging (circle) was distinctly detected.

The cell uptake and intracellular distribution of cRGD-encoded LQNBs with 530 nm QDs were evaluated by confocal laser scanning microscopy (CLSM). Endocytosis-mediated intracellular trafficking of ligands *via* the $\alpha_v\beta_3$ receptor of MCF-7 cells and the $\alpha_v\beta_5$ integrin receptor into the perinuclear region of HeLa cells was documented, which is devoid of the functional $\alpha_v\beta_3$ receptor. However, for the HeLa cells, which express the $\alpha_v\beta_3$ low level, an invasive potential lower than MCF-7 cells was demonstrated.[31] Fig. 4a and Fig. S6† show the cell uptake after incubation for a period of 2 h. The cRGD-free LQNBs took by MCF-7 and HeLa cells showed poor green fluorescence, which seemed to be arrested only on the surface of MCF-7 and HeLa cells (Fig. S6a).† In comparison, a significant difference in cellular uptake for the cRGD-encoded LQNBs by MCF-7 and HeLa cells for 2 h was determined, as shown in Fig. 4a, respectively. Numerous regions of strong green fluorescence emission was displayed on the surface and the cytoplasm regions of the MCF-7 cells and some of them were closed to the nucleus (Fig. S6b).† However, poor green fluorescent illuminations presented in the regions of cytoplasm and surface of HeLa cells (Fig. S6c).† It can be concluded that the cRGD peptide on LQNBs surface was responsible for cell uptake behavior for those $\alpha_v\beta_3$-expressing cells.

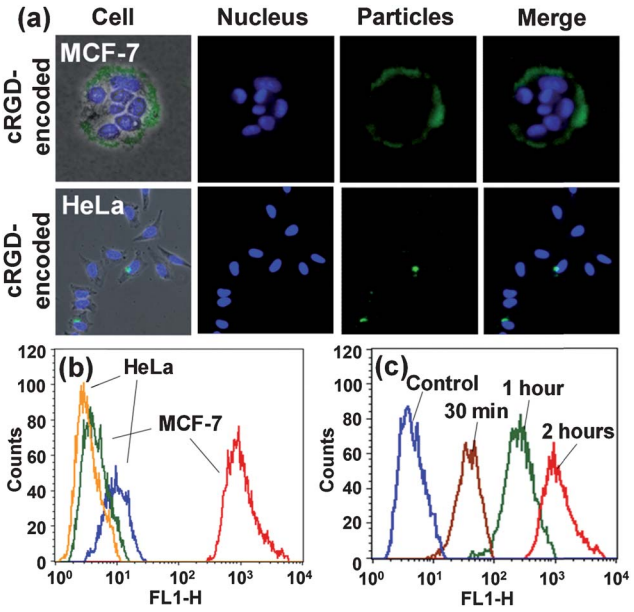

Fig. 4 (a) Cell uptake for an incubation of 2 h with cRGD-encoded LQNBs to MCF-7 and HeLa cells. The cell nucleus is stained with DAPI (blue) and LQNBs emitted light at 530 nm (green). (b) Quantitative flow cytometric data show the fluorescence brightness and uniformity levels of cRGD-free and cRGD-encoded LQNBs uptake by MCF-7 and HeLa cells for incubation of 2 h. (c) Flow cytometry analysis for the cRGD-encoded LQNBs accumulated in MCF-7 cells for an incubation of 30 min, 1 h and 2 h.

Further investigation using flow cytometry toward the LQNBs with MCF-7 and HeLa cells is shown in Fig. 4b. The cRGD-free LQNBs taken by HeLa (orange) and MCF-7 (green) displayed uniform signal intensities but for the cRGD-encode LQNBs taken by MCF-7 (red), the signal intensity was 100 times higher than that taken by HeLa cells (blue). The comparison strongly indicated that the cRGD-encoded LQNBs with the normal $\alpha_v\beta_3$ expression level of MCF-7 cells were taken more efficiently than the $\alpha_v\beta_3$ low expressing HeLa cells which expressed the $\alpha_v\beta_5$ integrin and correlated with low invasiveness. The cRGD-encoded LQNBs were capable of penetrating the MCF-7 cells, Fig. 4c, for a time period from 30 min to 2 h. The fluorescence intensity determined by flow cytometry rapidly increased, even clearly measurable at a starting 30-min period, further indicating highly efficient cellular internalization. This finding ascertains the advantageous design of LQNBs for cell-specific contrast imaging. Furthermore, the result of the MTT (3-(4,5-dimethyldiazol-2-yl)-2,5 diphenyl tetrazolium bromide) assay as a measure of metabolic competence of the cells with the nanobeads, LQNBs and 3-mercaptopropionic acid (MPA)-functionalized QDs of different concentrations was shown in Fig. S7.† The LQNBs demonstrated equivalent toxicity of the nanobeads, indicating a relatively low or little cytotoxicity of the newly-designed nanobeads to the MCF-7 cells. As a critical requirement for targeting and imaging modalities using quantum dots, a significant reduction of the cytotoxicity toward QDs through the use of the nanobeads can be critical. To this point, the multifunctionalized nanobeads designed and developed in this work are able to act as a potential contrast modality with improved not only imaging capability but also sufficient biocompatibility for medical practices.

In vivo fluorescence and bioluminescence imaging of the nude mice bearing MCF-7 xenografts implanted after intracortical injection with 50 μL cRGD-free and cRGD-encoded LQNBs was shown in Fig. 5a, 5b. For subcutaneously injected cRGD-free LQNBs, the fluorescence signals were rapidly decreasing at the tumor site after 1 day. The total flux (fluorescence intensity, TF) showed an initial value of 2.98×10^{10} p/s cm^{-2}/sr decreased nearly 100-fold to 3.06×10^{8} p/s cm^{-2}/sr after 7 days. In comparison, the cRGD-encoded LQNBs presented long lasting signals and the TF value showed an almost slow decrease tendency (by about 5-fold only) from 3.04×10^{10} p/s cm^{-2}/sr to 6.03×10^{9} p/s cm^{-2}/sr. The TF values of cRGD-encoded LQNBs were 20 times higher than cRGD-free LQNBs in 7 days. Clearly, the decrease in the rate of the fluorescent LQNBs in the tumor site is closely related to the cRGD peptide encoded or not. It is important to point out here that the cRGD-encoded LQNBs were responsible for the targeting behavior for those $\alpha_v\beta_3$-expressing MCF-7 tumors. Therefore, the cRGD-encoded LQNBs exhibited a moderately prolonged accumulation time at the MCF-7 tumor site but the cRGD-free LQNBs disappeared rapidly at the tumor site by blood circulation. Fig. 5c shows the major organs from sacrificing the nude mice bearing MCF-7 xenografts implanted after an intravenous injection with 50 μL cRGD-free and cRGD-encoded LQNBs. Fluorescence was barely detected in the heart and spleen, but was observed in the kidneys, liver, and lung. Because intravenously injected nanoparticles arrived at the heart as a first stop, followed by the lung, liver, and then other organs, we suspected that some aggregated nanoparticles were filtered by the lung, liver, and kidneys, resulting in an accumulated fluorescent signal. However, the higher fluorescence intensity was observed in the tumor after an intravenous injection with cRGD-encoded LQNBs as compared to the cRGD-free LQNBs. Furthermore, the accumulations of the fluorescent (cRGD-encoded LQNBs) became more pronounced after 3 days of injection. Thus, it can be conceivable that the cRGD-encoded LQNBs were able to provide targeting and imaging modalities for specific tumor cells.

Experiments

Materials

Cetyltrimethylammonium bromide (CTAB), ethanol (99.5%), n-butanol, n-octane, chloroform (99%), lysine, octadecyltrimethoxysilane, 2, 2′-azobis(2-amidinopropane) dihydrochloride (AIBA), 3-mercaptopropionic acid (MPA), 11-mercaptoundecanoic acid (MUA), polyethylene glycol 6000 (PEG), *N*-hydroxysuccinimide (NHS) and 1-ethyl-3-(3-dimethylaminopropyl)carbodiimide (EDC), were purchased from Aldrich. Tetraethylorthosilicate (TEOS) was purchased from Merck. Streptavidin-NH_2 and styrene monomer were purchased from Fluka. Core-shell quantum dots (ZnS-capped CdSe) were purchased from Ocean NanoTech. The QDs were coated with a layer of tri-n-octylphosphine oxide (TOPO) and the fluorescence quantum yield of QDs was about 60% at room temperature. Lipid-PEG_{2000}-COOH was purchased from Avanti Polar Lipids and cRGD-PEG_2-biotin was purchased from Peptides International.

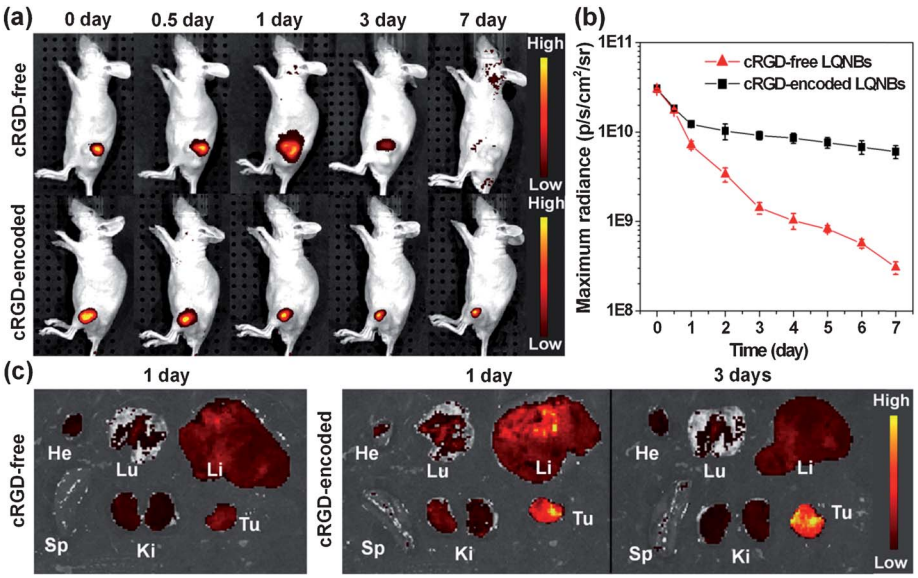

Fig. 5 (a) *In vivo* fluorescence imaging of nude mice bearing MCF-7 xenografts implanted after a subcutaneous injection with 50 μL cRGD-free and cRGD-encoded LQNBs in tumors. The total photon fluxes (TF) were determined at 0, 0.5, 1, 3 and 7 days using region-of-interest (ROI) measurement and expressed in photons/s. Color bar units are p/s cm^{-2}/sr, where p is for photon and sr is for steradian. (b) The change in luminescence over time for cRGD-free and cRGD-encoded LQNBs. (c) Photographic images of several organs and xenograft tumor from sacrificing the nude mice after an intravenous injection with cRGD-free and cRGD-encoded LQNBs for 1 and 3 days. The organs are heart (He), lung (Lu), liver (Li), spleen (Sp), kidneys (Ki) and tumor (Tu).

Characterization equipment

Nanostructures were investigated using scanning transmission electron (SEM, JSM-6700F, Japan), transmission electron microscopy (TEM, JEM-2010, Japan). PL spectroscopy (PL, Fluorescence Spectrophotometer F-4500, Hitachi, Japan) was used to characterize the fluorescence intensities of QD and LQNBs. True-color fluorescence images of LQNBs were obtained with an inverted Nikon microscope (Nikon TE-2000U, Japan) and a digital camera (Nikon DI). Broad-band excitation in the near-UV range (330–385 nm) was provided by a 100 W mercury lamp. A high-numerical-aperture (NA = 1.4, 100X), oil-immersion objective was used. The *in vivo* fluorescence imaging used an IVIS spectrum system (IVIS Imaging System 200 Series, Caliper Life Sciences, USA) and the collected images were analyzed by living image software version 3.0 (Xenogen).

Synthesis of hydrophobic porous nanobeads (NBs)

Cetyltrimethylammonium bromide (CTAB, 300 mg) was dissolved in a mixture of 45 ml octane and 96 ml dilute water at 70 °C. After stirring magnetically for 20 min, 8.5 ml styrene monomer, 66 mg lysine, 3000 mg tetraethylorthosilicate (TEOS), and 115 mg AIBA were subsequently added to the system and stirred magnetically for 4 h. After that, the heating was stopped and the suspension was cooled naturally to room temperature. The products were collected by centrifugation at 6000 rpm for 10 min and then washed 3 times with an excess of pure methanol. Finally the template was completely removed by heat treatment at 600 °C under atmospheric conditions.[32] The products, 500 mg mesoporous beads, were redispersed into a mixture of 3 ml octadecyltrimethoxysilane and 10 ml toluene. After stirring magnetically for 96 h at room temperature, the products were collected by centrifugation at 6000 rpm for 10 min and then redispersed into n-butanol.

Hydrophobic porous nanobeads incorporation of quantum dots and lipid-PEG_{2000}-COOH coating (LQNBs)

Incorporation of QDs was achieved by swelling the nanoporous beads in a solvent mixture containing 5% (vol/vol) chloroform and 95% (vol/vol) n-butanol, and then by adding a controlled amount of ZnS-capped CdSe QDs to the mixture. After stirring magnetically for 2 h, the products were collected by centrifugation at 8000 rpm for 10 min and were then redispersed into n-butanol (1 ml). Lipid-PEG_{2000}-COOH (3 mg) was added to the solution and sonicated for 3 min. Excess lipid were purified out from the solubilized beads with incorporation of QDs using repeated centrifugation at 8000 rpm for 10 min. The purified nanoparticles were redispersed in DI water.

Bioconjugate formation and cRGD-encoded

The LQNBs were activated by sonicating with 2 ml of 0.5% EDC containing *N*-hydroxysuccinimide (NHS) (0.2 wt%) aqueous solution. After stirring magnetically for 30 min, the nanoparticles were calibrated with sodium acetate buffer (pH 4.5). Streptavidin-NH_2 (0.1 mg mL^{-1}) in the same buffer solution was then applied for immobilization. At saturation, the nanocapsules were washed with distilled water. The cRGD-PEG_2-biotin was used to form a noncovalent biotin–streptavidin bridge for direct sensing of recombinant prion protein, the streptavidin surface of nanobeads was directly exposed to cRGD-PEG_2-biotin (0.05 mg mL^{-1}) in PBS buffer for incubation.[33]

Quantum yield measurement

The photoluminescence quantum yields (QY) of the samples were determined from eqn (2):

$$\text{Quantum yield (QY)}\% = Q_{st}(A_{st}/A_s)(D_s/D_{st}) \quad (2)$$

Here, Q_{st} is the quantum yield of the standard substance, Rhodamine B, known to be 0.31 in H_2O; A_{st} and A_s are the absorbance values of the Rhodamine B solution and the samples, respectively, at a wavelength of 514 nm; and D_s and D_{st} are the corresponding integrated wavenumber values for the sample and Rhodamine B, respectively, in the PL spectra.

The volume fraction of quantum dots in the nanobeads

The atomic concentration fraction of cadmium (Cd) to silicon (Si) which is 0.0255 was analyzed from inductively coupled plasma (ICP). The volume fraction of QDs (CdSe) is determined using eqn (3):

$$\frac{\text{Cd(ppm)}}{\text{Si(ppm)}} = \frac{\text{Cd(mmol)}}{\text{Si(mmol)}} = \frac{\text{Cd(mol)}}{\text{Si(mol)}} = 0.0255$$

$$\frac{\text{CdSe(v\%)}}{\text{SiO}_2\text{(v\%)}} = \frac{\text{CdSe}\left(\frac{\text{gcm}^3}{\text{g}}\right)}{\text{SiO}_2\left(\frac{\text{gcm}^3}{\text{g}}\right)} = \frac{\frac{\text{CdSe(mol)}}{\text{D}_{\text{CdSe}}} \text{ x } m_{\text{CdSe}}}{\frac{\text{SiO}_2\text{(mol)}}{\text{D}_{\text{SiO}_2}} \text{ x } m_{\text{SiO}_2}} = \frac{\text{Cd(mol)} \text{ x } \frac{m_{\text{CdSe}}}{m_{\text{Cd}}} \text{ x } \frac{m_{\text{CdSe}}}{D_{\text{CdSe}}}}{\text{Si(mol)} \text{ x } \frac{m_{\text{SiO}_2}}{m_{\text{Si}}} \text{ x } \frac{m_{\text{SiO}_2}}{D_{\text{SiO}_2}}} = 0.0294 = 2.94\% \quad (3)$$

where m_{Cd} (112.41), m_{CdSe} (191.37), m_{Si} (28.08) and m_{SiO_2} (60.08) are the molecular weight of Cd, CdSe, Si and SiO_2, respectively. D_{CdSe} (5.816 g cm^{-3}) and D_{SiO_2} (2.648 g cm^{-3}) are the density of CdSe and SiO_2, respectively.

Porous nanobeads embedded multicolor quantum dots

Three quantum dots (having green, yellow and red emissions) were mixed by a different ratio. Furthermore, incorporation of QDs was achieved by swelling the nanoporous beads in a solvent mixture containing 5% (vol/vol) chloroform and 95% (vol/vol) n-butanol, and then by adding a controlled amount of differently mixed ratio QDs to the mixture. After stirring magnetically for 2 h, the products were collected by centrifugation at 8000 rpm for 10 min

Quantum dots surface modified by tranditional molecules

The hydrophobic quantum dots were dispersed in chloroform. Three kinds of tranditional surface modified molecules, such as 3-mercaptopropionic acid (MPA), 11-mercaptoundecanoic acid (MUA) and polyethylene glycol 6000 (PEG) were individually added in DI water and mixed in a molar ratio of 100 : 1 to QDs. The mixture was vortexed and sonicated for 3 min. Chroloform was slowly evaporated under vacuum and the solution was centrifuged for 10 min at 12000 rpm to collect the product (repeat three times). The resulting MUA-QDs, MPA-QDs and PEG-QDs were readily resuspended into DI water. For QDs coated with SiO_2, 1.3 mL of IGEPAL CO-520 was added to 10 mL of cyclohexane, followed by the addition of 2 nmol of QDs (in 100 μL chloroform), 80 μL TEOS, and 150 μL ammonia aqueous solution (30%). Between each chemical addition, the reaction mixture was stirred for 15 min. The products (QDs@SiO_2) were collected by centrifugation at 4000 rpm for 10 min and resuspended into DI water.

Cell culture

MCF-7 (HeLa), human breast cancer (human cervix cancer) cells were maintained in DMEM (Dulbecco's modified Eagle's medium) containing 10% fetal bovine serum, 100 units/ml penicillin, and 100 μg ml^{-1} streptomycin. The cells were cultured with a complete medium at 37 °C in a humidified atmosphere of 5% CO_2 in air. For all experiments, cells were harvested from subconfluent cultures by use of trypsin and were resuspended in a fresh complete medium before plating. A comparison of *in vitro* cytotoxicity of QNBs with different concentrations was performed on MCF-7 cells with an *in vitro* proliferation method using MTT. Briefly, 10^4 cells were plated in 96-well plates to allow the cells to attach and then be exposed to the serial concentrations of QNBs at 37 °C. After the QNBs incubated with cells for 24 h, 20 μL of MTT solution was added and incubated for another 2 h. Then, the medium was replaced with 200 μL of DMSO, and the absorbance was monitored using a Sunrise absorbance microplate reader at dual wavelengths of 570 and 650 nm. To estimate the cellular uptake of the nanocarriers, the green emitting QDs were loaded into nanobeads (cRGD-free or cRGD-encoded LQNBs) for the study. The cRGD-free or cRGD-encoded LQNBs were incubated with the MCF-7 and HeLa cells for 2 h and then studied by CLSM and flow cytometry. On the other experimental strategy, the cRGD-encoded LQNBs were incubated with MCF-7 for different periods of time and measured by flow cytometry.

In vivo experiments

Using protocols approved by the Department of Life Science of the National Chiao Tung University, the LQNBs were injected into 6- to 8-week-old nude mice subcutaneously. Two sets of LQNBs (50 μL each)—one tagged with green QDs, the other orange-red QDs—were injected at two locations. Fluorescent images were recorded by IVIS Spectrum (IVIS Imaging System 200 Series, Caliper Life Sciences, USA). Living Image software Version 3.0 (Xenogen) was used to acquire and quantitate the fluorescence. The images showing QD530 and QD600 fluorescence were captured using excitation (Ex), 500 nm and emission (Em), 540 nm/600nm. Spectrally unmixed images were captured using a sequence of Ex, 500 nm and Em, 540 nm/560 nm/580 nm/

600 nm. For advanced fluorescence imaging, the IVIS Spectrum used *epi*-illumination (from the top) to illuminate *in vivo* fluorescent sources. After whole-body imaging, the mice were euthenized by overdosed CO_2.

Subcutaneous tumors were induced in either the left hind flank of nude mice after injection of about ten million cells (MCF-7) in 0.1 mL media. The tumors were allowed to grow to $\sim$100 mm^3 before experimentation. The MCF-7 xenograft nude mice were given a single injection of the cRGD-free and cRGD-encoded LQNBs *via* an intracortical injection. The concentration of the particles (cRGD-free and cRGD-encoded LQNBs) administered was 0.5 μM given in 50 μL injection. At various time points after injection, they were imaged ventrally using the IVIS system (Caliper Life Science). Living Image software Version 3.0 (Xenogen) was used to acquire and quantitate the fluorescence. The images showing QD530 fluorescence was captured using Ex, 500 nm and Em, 540 nm.

Conclusions

Highly biocompatible cRGD-encoded lipid-coated QDs tagged porous nanobeads (cRGD-encoded LQNBs) were successfully developed for cancer targeting and imaging *in vitro* and *in vivo*. The larger pores of the octadecyltrimethoxysilane modified nanobeads facilitated the internalization and stabilization of QDs. The QDs tagged nanobeads showed high chemical stability and a wide spectrum of multiplex color codings. *In vivo* and *in vitro* imaging studies showed a relatively sharp, stable and distinguishable contrast modality. Furthermore, cRGD-encoded LQNBs demonstrated a technical potential for visualizing the variations of uptake behavior between MCF-7 and HeLa cells, which may enable a further understanding on the cellular behavior on a nanometric-to-molecular scale. In MCF-7 xenograft nude mice, the cRGD-encoded LQNBs also exhibited long-lasting signals at the tumor site. With their nanostructural features, the cRGD-encoded LQNBs are expected to offer greater advantages over a wide range of targeting and cellular imaging modality for minimally invasive nano-imaging and nanodiagnosis applications.

Acknowledgements

This work was financially supported by the National Science Council of the Republic of China, Taiwan under Contract of NSC 99-2221-E-009-070-MY3 and NSC 99-2113-M-009-013-MY2. This work is also supported by "Aim for the Top University Plan" of the National Chiao Tung University and Ministry of Education, Taiwan, R.O.C.

References

1 I. J. Iwuchukwu, M. Vaughn, N. Myers, H. O'Neill, P. Frymier and B. D. Bruce, *Nat. Nanotechnol.*, 2010, **5**, 73.
2 U. Biermann, U. Bornscheuer, M. A. R. Meier, J. O. Metzger and H. J. Schafer, *Angew. Chem., Int. Ed.*, 2011, **50**, 3854.
3 S. Febvay, D. M. Marini, A. M. Belcher and D. E. Clapham, *Nano Lett.*, 2010, **10**, 2211.
4 B. Städler, A. D. Price and A. N. Zelikin, *Adv. Funct. Mater.*, 2011, **21**, 14.
5 B. M. Venkatesan and R. Bashir, *Nat. Nanotechnol.*, 2011, **6**, 615.
6 D. Shi, N. M. Bedford and H. S. Cho, *Small*, 2011, **7**, 2549.
7 G. Maltzahn, J. H. Park, K. Y. Lin, N. Singh, C. Schwöppe, R. Mesters, W. E. Berdel, E. Ruoslahti, M. J. Sailor and S. N. Bhatia, *Nat. Mater.*, 2011, **10**, 545.
8 K. Li and B. Liu, *J. Mater. Chem.*, 2012, **22**, 1257.
9 S. Shylesh, V. Schunemann and W. R. Thiel, *Angew. Chem., Int. Ed.*, 2010, **49**, 3428.
10 S. H. Hu, K. T. Kuo, D. M. Liu and S. Y. Chen, *Adv. Funct. Mater.*, 2009, **19**, 3396.
11 S. H. Hu, S. Y. Chen, C. S. Hsiao and D. M. Liu, *Adv. Mater.*, 2008, **20**, 2690.
12 X. Gao, Y. Cui, R. M. Levenson, L. W. K. Chung and S. Nie, *Nat. Biotechnol.*, 2004, **22**, 969.
13 Z. Liu, K. Yang and S. T. Lee, *J. Mater. Chem.*, 2011, **21**, 586.
14 J. D. Hartgerink, E. Beniash and S. I. Stupp, *Science*, 2001, **294**, 1684.
15 H. Cui, M. J. Webber and S. I. Stupp, *Biopolymers*, 2010, **94**, 1.
16 S. H. Hu, D. M. Liu, W. L. Tung, C. F. Liao and S. Y. Chen, *Adv. Funct. Mater.*, 2008, **18**, 2946.
17 B. Atmaja, B. H. Lui, Y. Hu, S. E. Beck, C. W. Frank and J. R. Cochran, *Adv. Funct. Mater.*, 2010, **20**, 4091.
18 R. J. Hickey, A. S. Haynes, J. M. Kikkawa and S. J. Park, *J. Am. Chem. Soc.*, 2011, **133**, 1517.
19 Z. Zhelev, H. Ohba and R. Bakalova, *J. Am. Chem. Soc.*, 2006, **128**, 6324.
20 C. Wu, Y. Jin, T. Schneider, D. R. Burnham, P. B. Smith and D. T. Chiu, *Angew. Chem., Int. Ed.*, 2010, **49**, 9436.
21 X. Gao and S. Nie, *Anal. Chem.*, 2004, **76**, 2406.
22 X. Gao and S. Nie, *J. Phys. Chem. B*, 2003, **107**, 11575.
23 E. Tasciotti, X. Liu, R. Bhavane, K. Plant, A. D. Leonard, B. K. Price, M. M. C. Cheng, P. Decuzzi, J. M. Tour, F. Robertson and M. Ferrari, *Nat. Nanotechnol.*, 2008, **3**, 151.
24 J. S. Ananta, B. Godin, R. Sethi, L. Moriggi, X. Liu, R. E. Serda, R. Krishnamurthy, R. Muthupillai, R. D. Bolskar, L. helm, M. Ferrari, L. J. Wilson and P. Decuzzi, *Nat. Nanotechnol.*, 2010, **5**, 815.
25 Y. Chen, H. Chen, S. Zhang, F. Chen, L. Zhang, J. Zhang, M. Zhu, H. Wu, L. Guo, J. Feng and J. Shi, *Adv. Funct. Mater.*, 2011, **21**, 270.
26 P. J. Chen, S. H. Hu, C. S. Hsiao, Y. Y. Chen, D. M. Liu and S. Y. Chen, *J. Mater. Chem.*, 2011, **21**, 2535.
27 J. Liu, S. Z. Qiao, Q. H. Hu and G. Q. Lu, *Small*, 2011, **7**, 425.
28 T. Kim, E. Momin, J. Choi, K. Yuan, H. Zaidi, J. Kim, M. Park, N. Lee, M. T. McMahon, A. Q. Hinojosa, J. W. M. Bulte, T. Hyeon and A. A. Gilad, *J. Am. Chem. Soc.*, 2011, **133**, 2955.
29 X. Hu and X. Gao, *ACS Nano*, 2010, **4**, 6080.
30 M. Han, X. Gao, J. Z. Su and S. Nie, *Nat. Biotechnol.*, 2001, **19**, 631.
31 K. Braun, M. Wiessler, R. Pipkorn, V. Ehemann, T. Bauerle, H. Fleischhacker, G. Muller, P. Lorenz and W. Waldeck, *Int. J. Med. Sci.*, 2010, **7**, 326.
32 A. B. D. Nandiyanto, S. G. Kim, F. Iskandar and K. Okuyama, *Microporous Mesoporous Mater.*, 2009, **120**, 447.
33 M. Shi, J. Lu and M. S. Shoichet, *J. Mater. Chem.*, 2009, **19**, 5485.